State-Independent Ionic Conductivity

Authors: J. Barclay[1,2], J. M. Williamson[2], H. Litt[3], S. J. Cowling[1], K. Shimizu[4], A. A. Freitas[4], S. Poppe[5], J. Sturala[2,6], Y. Sun[2], M. Kohout[7], A.-J. Avestro[1,8], J. N. Canongia Lopes[4], C. Groves[9], J. C. Jones[3], P. R. McGonigal[1,2,8,*]

Affiliations:

[1]Department of Chemistry, University of York; York, United Kingdom, YO10 5DD.

[2]Department of Chemistry, Durham University; Durham, United Kingdom, DH1 3LE.

[3]School of Physics and Astronomy, University of Leeds; Leeds, United Kingdom, LS2 9JT.

[4]Centro de Química Estrutural, Institute of Molecular Sciences, Instituto Superior Técnico, Universidade de Lisboa, 1049 001 Lisboa, Portugal

[5]Department of Chemistry, Martin Luther University Halle-Wittenberg; Halle, Germany, 06120.

[6]Department of Inorganic Chemistry, University of Chemistry and Technology; Prague, Czech Republic, 166 28 Praha 6.

[7]Department of Organic Chemistry, University of Chemistry and Technology; Prague, Czech Republic, 166 28 Praha 6.

[8]Department of Chemistry, University of Oxford, Oxford, United Kingdom, OX1 3TA.

[9]Department of Engineering, Durham University; Durham, United Kingdom, DH1 3LE.

*Corresponding author. paul.mcgonigal@chem.ox.ac.uk

Abstract: Liquids lend themselves to high ionic conductivities because of their molecular-level positional and orientational disorder, which enables the free movement of ions. However, there is an unavoidable steep drop in ionic conductivity upon phase transitions from a fluid state to the more ordered solid state. We describe organic salts that maintain the same ionic conductivity mechanism across transitions between three states of matter, from an initial isotropic liquid to liquid crystalline state and then to a crystalline solid. We achieve this property by minimizing the ion-pairing interactions between mobile ions and highly diffuse counterions that assemble in a stepwise manner to preserve conformational flexibility across phase transitions. This state-independent ionic conductivity opens up opportunities to exploit liquid-like ionic conductivity in organic solids.

One-Sentence Summary: Combining weak ionic interactions and structural flexibility preserves liquid-like conduction in organic solids.

Main Text:

In fluids, the energy barrier to ion diffusion is typically governed by the motion of the ions themselves as they hop between energetically favorable sites in the surrounding medium (*1, 2*). The diffusion of ions typically follows an Arrhenius relationship, where the logarithm of ionic conductivity ($\log(\sigma)$) varies linearly with the inverse of temperature ($1/T$). Certain inorganic solids act as super-ionic conductors, displaying conductivities as high as inorganic melts by providing pathways for the concerted migration of multiple ions (3). However, conventional organic fluid-phase electrolytes (COEs) undergo a steep decrease (Fig. 1A, blue line) in their ionic conductivity at the phase transition from fluid to solid (*4*–*7*), which is usually accompanied by a loss of the Arrhenius behavior and a dramatic decrease in ion mobility, indicating a change in conduction mechanism. The ion diffusion enters a viscosity-controlled regime described by the Vogel–Tamman–Fulcher relationship (*8*, 9) and the COEs undergo progressively sharper declines in their ionic conductivity at lower temperatures (Fig. 1A). Thus it remains a challenge to translate electrolyte properties from the fluid phase to the solid state because the mechanism of ion diffusion is not conserved upon phase transition in conventional organic materials (*8*–10).

We envisaged that this challenge could be overcome when the following design criteria (Fig. 1B) are met: (i) the cationic and anionic components of an electrolyte interact weakly with little or no orientational and positional preference relative to one another, (ii) in the solid state, one component (either the cation or anion) assembles into a lattice that contains numerous energetically near-equivalent sites (*11*, *12*) to accommodate its counterion, while still (iii) retaining structural degrees of freedom (*13*), thereby enabling the diffusion of the counterion through the solid network to follow the same mechanism as the isotropic liquid. As a practical design consideration, we postulated that conditions *ii* and *iii* are favored by salts that are predisposed to having an intermediate liquid crystal phase to allow order to be introduced in a stepwise manner as the electrolyte transitions from a fluid to a solid, thereby retaining some structural flexibility (*7*, *11*, *14*).

We report a series of organic salts (Fig. 1C) based on these design criteria that function as state-independent electrolytes (SIEs). They exhibit continuous, isotropic Arrhenius behavior across phase boundaries (Fig. 1A, orange line), indicating that they experience the same energy barriers to ion diffusion, and thereby retain their ionic conductivities, across three different states—isotropic liquid (Iso), liquid crystal (LC), and crystalline solid (C).

Results

We synthesized a series (Fig. 1C) of tris(trialkoxylphenyl) cyclopropenium salts (**SIE*n*·**X), each bearing nine equivalent linear alkyl chains of *n* carbon atoms in length. The triskelion-like molecular design arranges these conformationally flexible alkyl chains around the periphery of a rigid aromatic core with a cyclopropenium ring at its center (*15*–18), giving the molecules the characteristic structural features of a discotic mesogen (*19*). As a stable aromatic carbocation (*20*, *21*) with threefold rotational symmetry, the extension of the cyclopropenium π-system through the three coplanar trialkoxyphenyl groups allows a high degree of charge delocalization (*22*, 23). Therefore, anions would be expected to interact weakly around the periphery of the **SIE*n*$^+$** core.

SIEn·X salts have extremely weak ion-pairing interactions

Density functional theory (DFT) modelling (Fig. 1D) of the electrostatic surface potential (ESP) of the **SIE8**$^+$ cation confirms that the positive charge is shared evenly by its three trialkoxyphenyl rings. Notably, the charge density at the center of the rigid aromatic core is lower than that found around its periphery—the ESP is just 230 kJ·mol^{-1} at the cyclopropenium, relative to a value of 254 kJ·mol^{-1} for the patches spanning the aromatic CH and aliphatic CH_2 groups either side of the *para*-ether oxygens. For context, these potentials are approximately half those of imidazolium and ammonium head groups commonly used in ionic liquids (both ~500 kJ·mol^{-1}).

The triskelion arrangement of these alkyl chains favors self-assembly of the **SIE*n***$^+$ cations with their charge-bearing aromatic units embedded at the center of columnar stacks. Using DFT, we calculated (Fig. 1E) the optimum geometry of three self-assembled **SIE8**$^+$ discs, (**SIE8**$^+$)$_3$, as a minimal structural model for extended columnar stacking. By plotting the accessible surface for a 1.81 Å-radius sphere (the ionic radius of chloride) around the self-assembled column it becomes apparent that the core of the **SIE8**$^+$ disc in the middle of a column (Fig. 1E, orange) is sterically shielded from contacting chloride ions. Molecular dynamics (MD) simulations performed for **SIE10**·Cl in its crystal, liquid crystal and isotropic liquid phases (figs S82–83) reinforce this conclusion. The radial distribution functions for chloride (figs S84–88) indicate that the anions are mostly found (Fig. 1F) in a halo around the periphery of the aromatic core in all three phases.

Experimental evidence in support of the weak interaction between a **SIE*n***$^+$ cation and its halide counterion was obtained using X-ray photoelectron spectroscopy (XPS) to analyze the surface of a solid sample of **SIE10**·Cl (Fig. 2A). In the high-resolution chlorine 2p region, the most intense $2p_{3/2}$ peak appears with an extraordinarily low binding energy of 196.0 eV. This binding energy is indicative (*24*) of a non-coordinated chloride ion, c.f. 198.6 eV for LiCl, consistent with the DFT and MD predictions. A second, less intense $2p_{3/2}$ peak at 199.7 eV suggests that, at the surface of the sample at least, there are also some chloride ions that experience stronger ion pairing, which we attribute to interactions with exposed discs at the ends of **SIE*n***$^+$ columns at the surface of the sample. Single crystal X-ray diffraction of an analog lacking long alkyl chains, **SIE1**·Cl, also confirms (fig S76) that face-to-face interactions of the cyclopropeniums exclude the halide ions, which are disordered at sites outside the periphery of the aromatic core. Although each of the discs are positively charged, there is precedent that the coulombic repulsion between cyclopropenium cations can be overcome by their attractive dispersion interactions (*25*). Overall, the X-ray data and modelling show that columns of the **SIE*n***$^+$ cations interact extremely weakly with halide counterions, meeting the first of our design criteria.

Structural flexibility is retained in the solid state

Upon heating and cooling, the **SIE*n***·X materials undergo various phase transitions. Differential scanning calorimetry (DSC) shows that the chloride (Fig. 2B) and bromide salts (Table 1) are all solids at room temperature. They each undergo a phase transition to an isotropic liquid phase above ~50–85 °C depending on the alkyl chain length and counterion. The isotropic liquid phase of **SIE12**·Cl has a viscosity (table S3) of 91 mPa·S^{-1}, which is typical for an ionic liquid (*26*). Using polarized optical microscopy (POM), we identified the presence of an intermediate liquid crystal phase for each of the **SIE10**$^+$ (fig S39), **SIE12**$^+$ (Fig. 2C), and **SIE14**$^+$ (fig S41) chloride salts. Maltese cross textures observed in the POM images are characteristic of hexagonal columnar (Col_{hex}) mesophase structures, which is consistent with the self-assembly of **SIE*n***$^+$

discs into columns by cofacial stacking (Fig. 1E). At lower temperatures, we induce phase transition to the solid state (Fig. 2B,C). Assignment of the fluid-to-solid phase transitions is aided by identifying the largest phase transition enthalpies (*27*) by DSC upon heating and cooling (Fig. 2B, figs S36–38, Supplementary Data S1). The salts exhibit crystal–crystal phase transitions between up to three polymorphs, C-I, C-II, and C-III. This variation in phase structures across the series of **SIE*n***·X salts is summarized in Fig. 2D and Table 1.

Fourier transform infrared (FTIR) spectroscopy (Fig. 2E) and X-ray scattering measurements (Fig. 2F) give insights into the degree of order present in the different phases. A comparison of the ambient-temperature FTIR spectra of **SIE10**·Cl and **SIE18**·Cl shows higher wavenumber peaks arising from the C-I phase of **SIE10**·Cl relative to the C-II phase of **SIE18**·Cl (Fig. 2E). These CH_2 stretching vibrations are sensitive to the extent of lateral interactions between chains, so they give an indication of their packing density, disorder and conformational flexibility (*28*, *29*). The higher wavenumber peaks of **SIE10**·Cl indicate slightly reduced crystallinity and greater alkyl-chain flexibility in its C-I phase compared to the C-II phase of **SIE18**·Cl. Similarly, variable-temperature X-ray diffraction analysis (Fig. 2F) of **SIE14**·Cl is consistent with gradual increases in order (*30*) upon transitioning from its isotropic liquid phase to the liquid crystal, C-I, and C-II phases. The isotropic liquid gives a broad diffraction peak corresponding to the approximate diameter of the **SIE14**$^+$ disc (~31 Å) and another at ~4.5 Å that is typical of the distance between alkyl chains in a fluid. These peaks sharpen progressively through transitions to the liquid crystal, C-I, then C-II phases, alongside the appearance of new peaks in the 5–20 Å range for C-I and C-II, as well as signs of additional long-range order (>40 Å) in the C-II phase. The short-distance peak approaches 4.2 Å in C-II, which is indicative of closely packed alkyl chains. However, a shoulder remains at ~4.5 Å in both the C-I and C-II phases that suggests some alkyl-chain flexibility remains. X-ray scattering measurements of the other **SIE*n***·X salts reveal the same trends (fig S42–S49). Overall, these data show that the cationic components of these materials assemble into columnar structures that retain some structural flexibility in the solid state, meeting design criteria *ii* and *iii*.

Isotropic Arrhenius conductivity persists across phase boundaries

We measured the ionic conductivities (Fig. 3) of **SIE*n***·X thin films by performing a series of dielectric measurements (figs S58–S65), applying alternating currents of varying frequencies as the materials were cooled from their isotropic liquid phase (above 85 °C) to ambient temperature. We used the conductance values from the plateau (1–10 kHz) in the frequency sweeps to determine the conductivity arising predominantly from ionic charge carriers rather than electronic oscillations, which appear at higher frequencies. (*31*) We used glass cells (Fig. 3a) patterned with indium tin oxide (ITO) as a transparent electrode, which allowed us to determine the alignment of the materials by POM (fig S71). Samples of **SIE*n***·X were loaded into cells as isotropic liquids using capillary action to fill the cell gap (~20 μm). Upon cooling, we observed that the **SIE*n***$^+$ mesogens align parallel to the ITO surface, forming columns that are oriented perpendicular to the surface, as is commonly the case for discotic liquid crystals.

Using a sandwich cell architecture (Fig. 3A), we measured the ionic conductivity (Fig. 3B, figs S66–70) through the thin films, parallel to the alignment of these columns. At temperatures where the materials are in their isotropic liquid phase (Fig. 3B, black), we observe the expected Arrhenius relationship between σ and T. The Arrhenius behavior continues as the samples are cooled to their liquid crystal state (Fig. 3B, purple), indicating the partial orientational alignment of the **SIE*n***$^+$ cations does not change the activation energy barrier (E_a) to ion diffusion (Table 1). Upon phase transition of the **SIE16**·Cl and **SIE18**·Cl salts from their isotropic liquid phase

directly to their more ordered C-II phase, we observe abrupt decreases in conductivity that are similar to those (*4*–*7*, *32*) seen for COEs. However, the shorter chain compounds (n = 8–14) that form a C-I phase structure upon cooling to the solid state retain their Arrhenius behavior across this phase boundary (Fig. 3B, orange). The behavior is not limited to chloride ions, as we observe the same properties for the bromide salts of **SIE10**$^+$ and **SIE12**$^+$ (Fig. 3B, Table 1). By extending the measurements to sub-ambient temperatures, we observe that the uninterrupted Arrhenius behavior persists across additional phase transitions in some cases. There is no drop in conductivity as **SIE12**·Cl is cooled to its C-II phase (fig S69) or, remarkably, as **SIE8**·Cl is cooled past its C-III phase transition temperature (fig S72). **SIE14**·Cl on the other hand, exhibits a drop in conductivity (fig S70) as it enters its C-II phase, similarly to that observed for **SIE16**·Cl and **SIE18**·Cl.

We performed dielectric measurements (Fig. 3C) perpendicular to the columnar alignment of the thin films using an interdigitated electrode configuration (Fig. 3A). Comparing the parallel and perpendicular ionic conductivities of **SIE18**·Cl reveals the ionic conductivity becomes anisotropic as the material cools to its C-II phase, coinciding with the sharp decrease in ionic conductivity. By contrast, the parallel and perpendicular **SIE10**·Cl conductivity measurements give matching Arrhenius behavior across the phase transitions from the isotropic liquid to the C-I solid-state structure. Ion diffusion through **SIE10**·Cl remains isotropic (Fig. 3C) even as the packing structure of the **SIE10**$^+$ cation becomes anisotropic (Fig. 2D).

The observations of uninterrupted Arrhenius behavior upon cooling from an isotropic liquid to a solid precludes the possibility of the solid-state ionic conduction being limited to just the grain boundaries (*33*). The isotropic conductivity of **SIE10**·Cl in the solid state also rules out significant contributions from electrons hoping between π-systems, which come into close contact with one another along the axis of the columnar stacks (potentially contributing to $\sigma_{\parallel}$) but are insulated from one another by alkyl chains in the perpendicular directions ($\sigma_{\perp}$). Instead, the continuous variation of log(σ) we observe across phase transitions is characteristic of state-independent ionic conductivity. The same ion transport mechanism must govern the conductivity in the isotropic liquid, liquid crystal and C-I solid states. POM images confirm (fig S71) that the materials have undergone phase transitions to the solid state at the same temperatures determined by DSC.

The state-independent ionic conductivity persists on macroscopic length scales. Using a 0.7 cm-wide cell with two Pt electrodes (Fig. 3A), we performed electrochemical impedance spectroscopy and observed that **SIE12**·Cl retains continuous Arrhenius behavior as it cools from an isotropic liquid to its C-I solid phase (Fig. 3D). During this bulk measurement, the increased opacity of the sample as it undergoes phase transition to the solid is visible to the naked eye (Fig. 3D, inset). At 30 °C, the bulk conductivity of 2×10^{-7} S·cm^{-1} is comparable to glassy inorganic lithium phosphorus oxynitride (*34*), which is also an attractive low-cost, ambient stable electrolyte. If desired, the relatively low conductivities of the neat **SIE*n***·X materials could be increased by adding dopants (*4*, *5*, *35*) or optimizing the molecular design of the SIE, e.g., the number and lengths of alkyl chains or the size and symmetry of the aromatic core. Anion-conductive materials find uses in organic photovoltaics (*36*) and anion shuttle batteries (*37*).

Mechanistic insights

The state-independent continuous isotropic Arrhenius conduction of the SIEs sets them apart from other electrolytes, which have traditionally been siloed into two classes: either those that function as fluids (i.e., salty solutions (*38*) or neat ionic liquids (*39*, 40)), or those that function in

the solid state (i.e., inorganics (*14*, *31*, *41*), polymers (*8*), and composites (*42*)). Individually, either of these two classes have benefits and drawbacks. Unlike solids, fluid-phase electrolytes typically form good interfacial contacts with electrodes and benefit from being flexible and lightweight, while solid-state electrolytes are considered safer than liquids because they are not prone to leakage and tend to be more robust towards thermal cycling. Consequently, research has been directed toward developing advanced electrolytes, such as quasi-solid polymer electrolytes (*43*, *44*), high-concentration electrolytes (*45*), organic ionic plastic crystals (*46*), other composites (*47*), and non-crystalline solids (*15*, *48*) that combine these favorable properties in a single material. A mechanistic understanding of SIEs could aid in designing electrolytes that can be cycled between fluid and solid states, taking advantage of the benefits of each without a large trade-off in performance.

Some mechanistic conclusions can be inferred from the observed conductivity trends of the **SIE*n***·X salts. Firstly, the ionic conductivity in the solid state must be dominated by diffusion of the halides (*49*) since any dielectric response arising from motion of the cation would be expected to be anisotropic on account of its columnar ordering. This mechanism is supported by MD simulations of solid **SIE10**·Cl run with a simulated electric field applied parallel ($E\parallel$) or perpendicular ($E\perp$) to the column axis (movie S1). While the **SIE10**$^+$ cations remain at the same sites during the simulation, the chloride ions hop between sites giving equivalent mean square displacement (MSD) under the $E\parallel$ or $E\perp$ field (Fig. 3E).

Secondly, a related mechanistic corollary is that the ionic conductivity of **SIE*n***·X materials must not only be dominated by chloride diffusion in the liquid crystal or solid phases, but also when they are isotropic liquids. Melting the materials to cause disassembly of the **SIE*n***$^+$ cations does not lead to a discernable change in the slope of $1/T$ versus $\log(\sigma)$, implying that the large cations do not contribute appreciably to the conductivity even when they have no orientational or positional order. Pulsed-field gradient ^{1}H NMR spectroscopy measurements (figs S31–34) show that, unlike typical columnar materials (*50*), the diffusion constants of **SIE10**·Cl and **SIE16**·Cl (table S1) do not increase substantially upon melting to the liquid phase. MD simulation of the liquid state of **SIE10**·Cl at 400 K shows (fig S92) that while there is a ~80% probability of the cations fully disassembling, there is some residual local structure with a ~20% probability of the cations being found as dimers.

Finally, the mechanism of halide diffusion is conserved between the isotropic liquid, liquid crystal, and C-I phases and must be minimally affected by the disassembly or assembly of the cationic component as the material is heated or cooled. The slopes of the Arrhenius plots (Fig. 3B) and, therefore, the E_a for ion diffusion (Table 1) remains constant over the temperature window investigated. Accordingly, we infer that the chloride ions responsible for the conductivity are those identified by XPS (Fig. 2A) as being particularly weakly coordinated (design criterion *i*). Their nonselective interactions with the cation at multiple sites around the self-assembled columns (criterion *ii*), as revealed by the ESP maps (Fig. 1D) and accessible surface area plots (Fig. 1E), mean that they are not constrained within the rigid, ordered region of the packing structure at the cores of the cyclopropenium discs. Instead, they can hop through the mildly electropositive alkyl chains around the periphery of the **SIE*n***$^+$ cations, which retain sufficient conformational flexibility (criterion *iii*) in the C-I phase (and even the C-II and C-III phases in some cases) such that there is no observable drop in conductivity.

Conclusions

In summary, we demonstrate a class of electrolytes that maintain the same mechanism of ionic conductivity across three distinct states of matter. By analyzing the characteristic molecular features of these organic salts and by contrasting the properties of their different packing structures, we have linked our design criteria to the mechanisms underpinning their state-independent ionic conductivity. In the present system, the anionic components are responsible for the conduction, which occurs isotropically, irrespective of whether the cationic components are disordered in the liquid state or ordered anisotropically as a solid. The design principles described here could also be employed to develop cation-conductive analogs. State-independent ionic conductivity of this kind offers an approach to devising and understanding electrolytes that bring together the beneficial aspects of fluids and solids.

References and Notes

1. M. Sotoudeh, *et al.*, Ion Mobility in Crystalline Battery Materials. *Adv. Energy Mater.* **14**, 2302550 (2024).
2. D. Lu, *et al.*, Ligand-channel-enabled ultrafast Li-ion conduction. *Nature* **627**, 101–107 (2024).
3. X. He, Y. Zhu, Y. Mo, Origin of fast ion diffusion in super-ionic conductors. *Nature Commun.* **8**, 15893 (2017).
4. D. R. MacFarlane, J. Huang, M. Forsyth, Lithium-doped plastic crystal electrolytes exhibiting fast ion conduction for secondary batteries. *Nature* **402**, 792–794 (1999).
5. Y. Shekibi, T. Rüther, J. Huang, A. F. Hollenkamp, Realisation of an all solid state lithium battery using solid high temperature plastic crystal electrolytes exhibiting liquid like conductivity. *Phys. Chem. Chem. Phys.* **14**, 4597–4604 (2012).
6. K. Romanenko, L. Jin, L. A. Madsen, J. M. Pringle, L. A. Odell, M. Forsyth, Anisotropic MRI contrast reveals enhanced ionic transport in plastic crystals. *J. Am. Chem. Soc.* **136**, 15638–15645 (2014).
7. M. A. Kolmangadi, *et al.*, Side Chain Length-Dependent Dynamics and Conductivity in Self-Assembled Ion Channels. *J. Phys. Chem. C.* **126**, 10995–11006 (2022).
8. Q. Zhao, S. Stalin, C. Z. Zhao, L. A. Archer, Designing solid-state electrolytes for safe, energy-dense batteries. *Nat. Rev. Mater.* **5**, 229–252 (2020).
9. K. M. Diederichsen, H. G. Buss, B. D. McCloskey, The Compensation Effect in the Vogel-Tammann-Fulcher (VTF) Equation for Polymer-Based Electrolytes. *Macromolecules* **50**, 3831–3840 (2017).
10. C. Y. Son, Z. G. Wang, Ion transport in small-molecule and polymer electrolytes. *J. Chem. Phys.* **153**, 100903 (2020).
11. Y. Zeng, *et al.*, High-entropy mechanism to boost ionic conductivity. *Science* **378**, 1320–1324 (2022).
12. G. Han, *et al.*, Superionic lithium transport via multiple coordination environments defined by two-anion packing. *Science* **383**, 739–745 (2024).
13. S. Krause, J. V. Milić, Functional dynamics in framework materials. *Commun Chem.* **6**, 151 (2023).
14. T. M. F. Restle, *et al.*, Super-Ionic Conductivity in ω-Li_9TrP_4 (*Tr* = Al, Ga, In) and Lithium Diffusion Pathways in Li_9AlP_4 Polymorphs. *Adv Funct. Mater.* **32**, 2112377 (2022).
15. B. A. Paren, R. Raghunathan, I. J. Knudson, J. L. Freyer, L. M. Campos, K. I. Winey, Impact of building block structure on ion transport in cyclopropenium-based polymerized ionic liquids. *Polym. Chem.* **10**, 2832–2839 (2019).
16. J. Litterscheidt, *et al.*, Self-Assembly of Aminocyclopropenium Salts: En Route to Deltic Ionic Liquid Crystals. *Angew. Chem. Int. Ed.* **59**, 10557–10565 (2020).
17. R. Walser-Kuntz, Y. Yan, Matthew S. Sigman, M. S. Sanford, A Physical Organic Chemistry Approach to Developing Cyclopropenium-Based Energy Storage Materials for Redox Flow Batteries. *Acc. Chem. Res.* **56**, 1239–1250 (2023).
18. M. Fink, J. Stäuble, M. Weisgerber, E. M. Carreira, Aryl Azocyclopropeniums: Minimalist, Visible-Light Photoswitches. *J. Am. Chem. Soc.* **146**, 9519–9525 (2024).
19. V. Percec, D. Sahoo, Discotic liquid crystals 45 years later. Dendronized discs and crowns increase liquid crystal complexity to columnar from spheres, cubic Frank-Kasper, liquid quasicrystals and memory-effect induced columnar-bundles. *Giant* **12**, 100127 (2022).
20. D. J. M. Lyons, R. D. Crocker, M. Blümel, T. V. Nguyen, Promotion of Organic Reactions by Non-Benzenoid Carbocyclic Aromatic Ions. *Angew. Chem. Int. Ed.* **56**, 1466–1484 (2017).

21. P. K. Saha, A. T. Turley, A. N. Bismillah, A. P. Monkman, D. S. Yufit, P. R. McGonigal, Rupturing Aromaticity by Periphery Overcrowding. *Nat. Chem.* **15**, 516–525 (2022).
22. R. Weiss, T. Brenner, F. Hampel, A. Wolski, The Consequences of an Electrostatic "Forced Marriage" between Two Electron-Rich Particles: Strained Ion Pairs. *Angew. Chem. Int. Ed.* **34**, 439–441 (1995).
23. S. Huang, J. Zheng, Z. Jiang, J. Liu, Y. Liu, Exploring the supramolecular chemistry of cyclopropeniums: halogen-bonding-induced electrostatic assembly of polymers. *Chem. Sci.* **14**, 9820–9826 (2023).
24. A. R. Santos, R. K. Blundell, P. Licence, XPS of guanidinium ionic liquids: A comparison of charge distribution in nitrogenous cations. *Phys. Chem. Chem. Phys*. **17**, 11839–11847 (2015).
25. A. J. Wallace, C. D. Jayasinghe, M. I. J. Polson, O. J. Curnow, D. L. Crittenden, Cyclopropenium Cations Break the Rules of Attraction to Form Closely Bound Dimers. *J. Am. Chem. Soc*. **137**, 15528–15532 (2015).
26. K. Paduszyński, U. Domańska, Viscosity of Ionic Liquids: An Extensive Database and a New Group Contribution Model Based on a Feed-Forward Artificial Neural Network. *J. Chem. Inf. Model.* **54**, 1311-1324, (2014).
27. W. E. Acree, J. S. Chickos, Phase Change Enthalpies and Entropies of Liquid Crystals. *J. Phys. Chem. Ref. Data* **35**, 1051–1330 (2006).
28. M. D. Porter, T. B. Bright, D. L. Allara, C. E. D. Chidsey, Spontaneously organized molecular assemblies. 4. Structural characterization of n-alkyl thiol monolayers on gold by optical ellipsometry, infrared spectroscopy, and electrochemistry. *J. Am. Chem. Soc*. **109**, 3559–3568 (1987).
29. H. Li, *et al.*, Alkylated-C_{60} based soft materials: Regulation of self-assembly and optoelectronic properties by chain branching. *J. Mater. Chem. C* **1**, 1943–1951 (2013).
30. A. M. Rich, *et al.*, Quantifying alkyl chain disorder in crystalline models of lipid bilayers using Raman spectroscopy. *J. Raman Spectrosc*. **50**, 63–73 (2019).
31. F. Kremer, S. A. Różański, The Dielectric Properties of Semiconducting Disordered Materials. In: F. Kremer, F., A. Schönhals, (eds) Broadband Dielectric Spectroscopy (2003). Springer, Berlin, Heidelberg.
32. J. Wang, J. Ding, O. Delaire, G. Arya, Atomistic Mechanisms Underlying Non-Arrhenius Ion Transport in Superionic Conductor $AgCrSe_2$. *ACS Appl. Energy Mater*. **4**, 7157–7167 (2021).
33. H. Zhu, X. Wang, R. Vijayaraghava, Y. Zhou, D. R. Macfarlane, M. Forsyth, Structure and Ion Dynamics in Imidazolium-Based Protic Organic Ionic Plastic Crystals. *J. Phys. Chem. Lett.* **9**, 3904–3909 (2018).
34. P. López-Aranguren, *et al.*, Crystalline LiPON as a Bulk-Type Solid Electrolyte. *ACS Energy Lett*. **6**, 445–450 (2021).
35. F. Makhlooghiazad, *et al.*, Zwitterionic materials with disorder and plasticity and their application as non-volatile solid or liquid electrolytes. *Nat. Mater*. **21**, 228–236 (2022).
36. M. Wang, *et al.*, An organic redox electrolyte to rival triiodide/iodide in dye-sensitized solar cells. *Nature Chem.* **2**, 385–389 (2010).
37. Y. Wang, *et al.*, Electrolyte design for rechargeable anion shuttle batteries. *eScience* **2**, 573–590 (2022).
38. K. Xu, Nonaqueous liquid electrolytes for lithium-based rechargeable batteries. *Chem. Rev*. **104**, 4303–4417 (2004).
39. T. Kato, M. Yoshio, T. Ichikawa, B. Soberats, H. Ohno, M. Funahashi, Transport of ions and electrons in nanostructured liquid crystals. *Nat. Rev. Mater*. **2** 17001 (2017).
40. L. Yu, G. Z. Chen, Ionic liquid-based electrolytes for supercapacitor and supercapattery. *Front. Chem*. **7**, 272 (2019).
41. J. C. Bachman, *et al.*, Inorganic Solid-State Electrolytes for Lithium Batteries: Mechanisms and Properties Governing Ion Conduction. *Chem. Rev*. **116**, 140–162 (2016).
42. Z. Zou, *et al.*, Mobile Ions in Composite Solids. *Chem. Rev*. **120**, 4169–4221 (2020).
43. N. M. Saidi, *et al.*, Enhancing the Efficiency of a Dye-Sensitized Solar Cell Based on a Metal Oxide Nanocomposite Gel Polymer Electrolyte. *ACS Appl. Mater. Interfaces*. **11**, 30185–30196 (2019).
44. X. He, *et al.*, Insights into the Ionic Conduction Mechanism of Quasi-Solid Polymer Electrolytes through Multispectral Characterization. *Angew. Chem. Int. Ed.* **60**, 22672–22677 (2021).
45. G. Jiang, *et al.*, Perspective on High-Concentration Electrolytes for Lithium Metal Batteries. *Small Struct*. **2**, 2000122 (2021).
46. H. Zhu, D. R. MacFarlane, J. M. Pringle, M. Forsyth, Organic Ionic Plastic Crystals as Solid-State Electrolytes. *Trends Chem*. **1**, 126–140 (2019).
47. T. J. Quill, *et al.*, An ordered, self-assembled nanocomposite with efficient electronic and ionic transport. *Nat. Mater.* **22**, 362–368 (2023).
48. Z. A. Grady, C. J. Wilkinson, C. A. Randall, J. C. Mauro, Emerging Role of Non-crystalline Electrolytes in Solid-State Battery Research. *Front. Energy Res*. **8**, 218, (2020).
49. L. Stolz, S. Hochstädt, S. Röser, M. R. Hansen, M. Winter, J. Kasnatscheew, Single-Ion versus Dual-Ion Conducting Electrolytes: The Relevance of Concentration Polarization in Solid-State Batteries. *ACS Appl. Mater. Interfaces*. **14**, 11559–11566 (2022).

50. S. V. Dvinskikh, I. Furó, H. Zimmermann, A. Maliniak, Molecular self-diffusion in a columnar liquid crystalline phase determined by deuterium NMR. *Phys. Rev. A.* **65**, 050702 (2002).
51. S. Dhingra, S. P. Gupta, A. Shah, D. P. Singh, S. K. Pal, Temperature-dependent hole mobility in pyrene–thiophene-based room-temperature discotic liquid crystals, *Chem. Commun.* **60**, 2922–2925 (2024).
52. R. Breslow, W. Chu, Thermodynamic determination of pKa's of weak hydrocarbon acids using electrochemical reduction data. Triarylmethyl anions, cycloheptatrienyl anion, and triphenyl- and trialkylcyclopropenyl anions. *J. Am. Chem. Soc.* **95**, 411–418 (1973).
53. D. Dunmur, K. Toriyama, Dielectric Properties, In: D. Demos, J. Goodby, G.W.Gray, H.-W., Speiss and V. Vill (eds), The Handbook of Liquid Crystals, Volume 1: Fundamentals (1998), Wiley VCH.
54. T. J. Phillips, J. C. Jones, D. G. McDonnell, On the influence of short range order upon the physical properties of triphenylene nematic discogens. *Liq. Cryst.* **15**, 203–215 (1993).
55. Gaussian 16, Revision C.01, M. J. Frisch, G. W. Trucks, H. B. Schlegel, G. E. Scuseria, M. A. Robb, J. R. Cheeseman, G. Scalmani, V. Barone, G. A. Petersson, H. Nakatsuji, X. Li, M. Caricato, A. V. Marenich, J. Bloino, B. G. Janesko, R. Gomperts, B. Mennucci, H. P. Hratchian, J. V. Ortiz, A. F. Izmaylov, J. L. Sonnenberg, D. Williams-Young, F. Ding, F. Lipparini, F. Egidi, J. Goings, B. Peng, A. Petrone, T. Henderson, D. Ranasinghe, V. G. Zakrzewski, J. Gao, N. Rega, G. Zheng, W. Liang, M. Hada, M. Ehara, K. Toyota, R. Fukuda, J. Hasegawa, M. Ishida, T. Nakajima, Y. Honda, O. Kitao, H. Nakai, T. Vreven, K. Throssell, J. A., Jr, Montgomery, J. E. Peralta, F. Ogliaro, M. J. Bearpark, J. J.; Heyd, E. N. Brothers, K. N. Kudin, V. N. Staroverov, T. A. Keith, R. Kobayashi, J. Normand, K. Raghavachari, A. P. Rendell, J. C. Burant, S. S. Iyengar, J. Tomasi, M. Cossi, J. M. Millam, M. Klene, C. Adamo, R. Cammi, J. W. Ochterski, R. L. Martin, K. Morokuma, O. Farkas, J. B. Foresman, D. J. Fox, Gaussian, Inc., Wallingford CT, 2016.
56. W. L. Jorgensen, D. S. Maxwell, J. Tirado-Rives, Development and Testing of the OPLS All-Atom Force Field on Conformational Energetics and Properties of Organic Liquids. *J. Am. Chem. Soc.* **118**, 11225−11236 (1996).
57. V. Lesch, *et al.*, Molecular dynamics analysis of the effect of electronic polarization on the structure and single-particle dynamics of mixtures of ionic liquids and lithium salts. *J. Chem. Phys.* **145**, 204507 (2016).
58. H. Bekker, *et al.*, Gromacs: A parallel computer for molecular dynamics simulations. *Physics Computing '92: Proceedings of the 4th International Conference Physics Computing*, 252–256 (1993).
59. H. Berendsen, D. Van der Spoel, R. Van Drunen. GROMACS: A message-passing parallel molecular dynamics implementation. *Comput. Phys. Commun.* **91**, 43–56 (1995).
60. D. Van der Spoel, E. Lindahl, B. Hess, G. Groenhof, A. E. Mark, H. J. C. Berendsen. GROMACS: Fast, flexible, and free. *J. Comput. Chem.* **26**, 1701–1718 (2005).
61. S. Páll, M. J. Abraham, C. Kutzner, B. Hess, E. Lindahl. Tackling exascale software challenges in molecular dynamics simulations with GROMACS. *Proc. of EASC 2015 LNCS* **8759**, 3–27 (2015).
62. M. J. Abraham, T. Murtola, R. Schulz, S. Páll, J. C. Smith, B. Hess, E. Lindahl. GROMACS: High performance molecular simulations through multi-level parallelism from laptops to supercomputers. *SoftwareX* **1–2**, 19–25 (2015).
63. W. Smith, T. R. Forester. *The DL_POLY Package of Molecular Simulation Routines*, v.2.2; The Council for The Central Laboratory of Research Councils; Daresbury Laboratory: Warrington, U.K., 2006.
64. L. Martínez, R. Andrade, E. G. Birgin, J. M. Martínez. Packmol: A package for building initial configurations for molecular dynamics simulations. *J. Comput. Chem.* **30**, 2157−2164 (2009).
65. A. A. H. Padua, K. Goloviznina, Z. Gong, agiliopadua/fftool: XML force field files (v1.2.1). Zenodo. https://doi.org/10.5281/zenodo.4701065, 2021.
66. K. Wendler, F. Dommert, Y. Y. Zhao, R. Berger, C. Holm, L. D. Site. Ionic liquids studied across different scales: A computational perspective. *Faraday Discuss.* **154**, 111–132 (2012).
67. I. V. Leontyev, A. A. Stuchebrukhova. Electronic continuum model for molecular dynamics simulations. *J. Chem. Phys.* **130**, 085102 (2009).
68. K. Shimizu, A. A. Freitas, J. N. Canongia Lopes. Structural characterization of the $[C_nC_1im][C_4F_9SO_3]$ ionic liquid series: Alkyl versus perfluoroalkyl side chains. *J. Mol. Liq.* **226**, 28–34 (2017).
69. P. J. Brown, A. G. Fox, E. N. Maslen, M. A. O'Keefe, T. M. Willis, In: E. Prince (ed.), International Tables for Crystallography, vol. C, International Union of Crystallography, Dordrecht, 554–595 (2004).
70. E. Lorch. Neutron diffraction by germania, silica and radiation-damaged silica glasses. *J. Phys. C: Solid State Phys*. **2**, 229 (1969).
71. M. Brehm, B. Kirchner. TRAVIS–A free Analyzer and Visualizer for Monte Carlo and Molecular Dynamics Trajectories. *J. Chem. Inf. Model*. **51**, 2007–2023 (2011).
72. M. Brehm, M. Thomas, S. Gehrke, B. Kirchner. TRAVIS–A Free Analyzer for Trajectories from Molecular Simulation. *J. Chem. Phys.* **152**, 164105 (2020).

Acknowledgments: We thank Gang Cheng for assistance with XPS, Douglas Carswell for assistance with DSC, Samuel Page for acquiring solid-state NMR, and John Slattery and Duncan Bruce for useful discussions.

Funding:

Engineering and Physical Sciences Research Council (EPSRC) SOFI CDT Studentship EP/L015536/1 (JMW, PRM)

EPSRC ReNU CDT Studentship EP/S0238361/1 (JB, CG, PRM)

EPSRC New Horizons Research Grant EP/V047817/1 (YS, PRM)

EPSRC Advanced Manufacturing Fellowship EP/S029214/1 (JCJ)

Northern Accelerator Feasibility Grant NACCF227 (JMW, PRM)

Faraday Institution Battery Study and Seed Research Project FIRG046 (PRM)

Royal Society International Collaboration Award ICA\R1\231091 (PRM)

Fundação para a Ciência e Tecnologia, FCT/MCTES, Portugal
CEEC contracts (IST-ID/100/2018 to K.S. and IST-ID/93/2018 to A.A.d.F.)
Projects grant UIDB/00100/2020 (https://doi.org/10.54499/UIDB/00100/2020) and LA/P/0056/2020 (https://doi.org/10.54499/LA/P/0056/2020)

Author contributions:

Conceptualization: PRM

Methodology: JMW, JB, HL, JS, YS, MK, AJA, JNCL, JCJ, PRM

Investigation: JMW, JB, HL, SP, SJC, KS, AAF, PRM

Funding acquisition: PRM, JCJ, CG

Project administration: PRM

Supervision: PRM, JCJ, CG, MK

Writing – original draft: PRM, JB, JMW, HL

Writing – review & editing: JB, JMW, HL, JS, YS, SJC, KS, AAF, MK, AJA, JNCL, CG, JCJ, PRM

Competing interests: The authors declare no competing interests.

Data and materials availability: Crystallographic data for **SIE1**·Cl are available from the Cambridge Crystallographic Data Centre (deposition number 2346813).

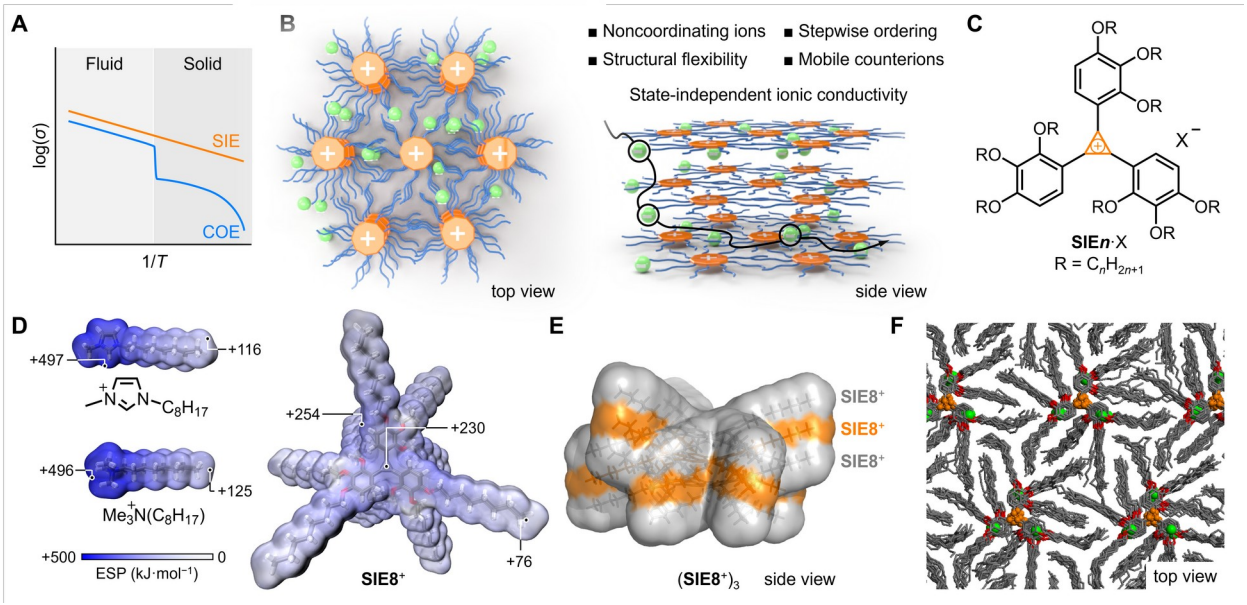

Fig. 1. Design elements for state-independent ionic conductivity. (**A**) The typical trend for change in σ with T of a COE is contrasted with that of a SIE. The conductivity of the COE drops abruptly upon phase transition from a fluid to the solid state as it undergoes a change in ionic conductivity mechanism, whereas ion diffusion within the SIE continues by the same mechanism across phase boundaries, leading to continuous Arrhenius behavior. (**B**) Schematic illustration of the SIE solid-state superstructure and properties. The mobile ions diffuse isotropically through an anisotropic columnar network of noncoordinating organic counterions, i.e., with equal energy barriers in all dimensions. The positional and orientational order of the organic counterion component is introduced in a stepwise manner as the isotropic liquid cools to a solid, retaining conformational flexibility in its alkyl chains. (**C**) The structural formula of the **SIE*n***·X series of SIEs. (**D**) Comparison of the calculated (B3LYP/6-31G(d,p)) ESPs of **SIE8**$^+$ and common cationic imidazolium and ammonium motifs used in ionic liquids and ionic liquid crystals shows the significant charge delocalization and three-fold rotational symmetry of the **SIE*n***$^+$ non-coordinating cations. The ESPs are plotted at an electron density isovalue of 0.001. (**E**) The surface accessible to a 1.81 Å-radius sphere (chloride radius) around a (**SIE8**$^+$)$_3$ trimer (B3LYP/

D3(BJ)/3-21G). The **SIE8**$^{+}$ discs at the top and bottom are grey and the middle disc is orange. (**F**) Snapshot of a MD simulation of the crystal phase of **SIE10**·Cl at 298 K. Cyclopropenium carbon atoms in orange, other carbon atoms in gray, oxygen atoms in red, chloride ions in green.

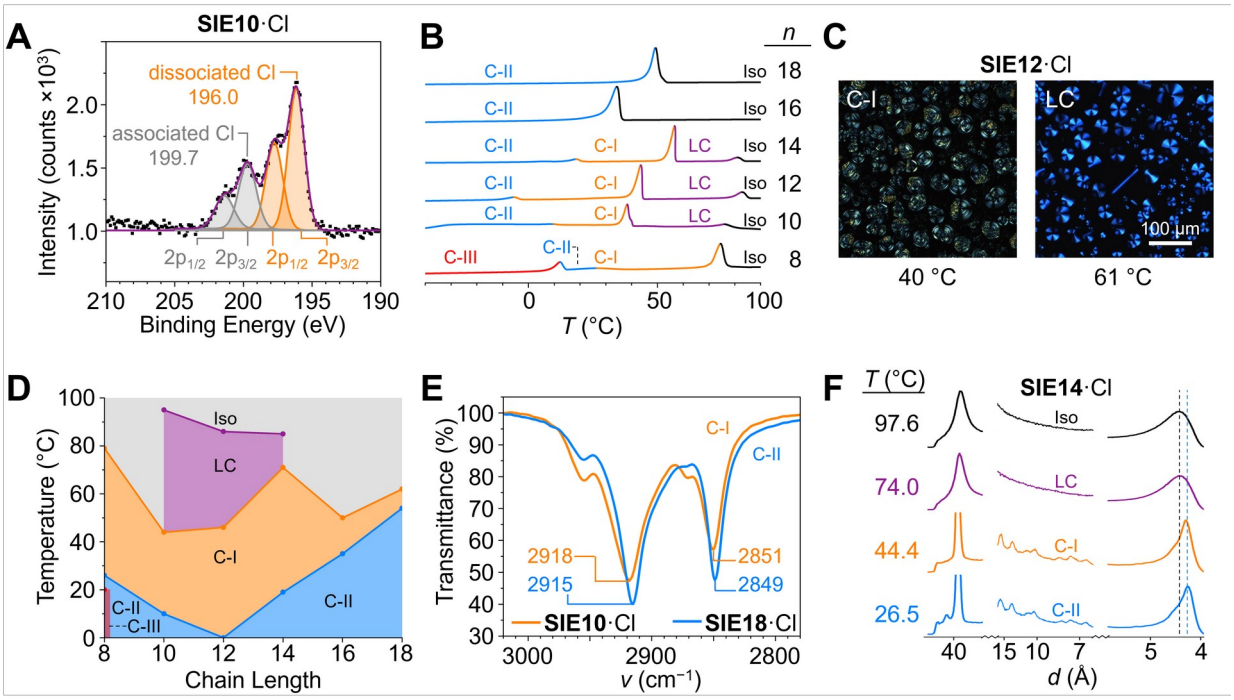

Fig. 2. Spectroscopic, thermal, and X-ray data show chloride dissociation and the differing levels of structural flexibility for the fluid and solid phases. (**A**) Cl2p region of the XPS spectrum of **SIE10**·Cl (23 °C) showing two chloride environments. Fitted gaussian peaks are shown in orange and grey, which combine to give the purple trace. (**B**) DSC curves for the **SIE*n***·Cl materials upon cooling. Phases are labelled as isotropic liquid (Iso), liquid crystal (LC) and crystal (C-I, C-II, and C-III). Intensities are normalized. (**C**) POM images of **SIE12**·Cl as a crystal (C-I) at 40 °C and showing a characteristic Col_{hex} liquid crystal texture at 61 °C. (**D**) Phase diagram for **SIE*n***·Cl materials upon heating. (**E**) Ambient (23 °C) FTIR spectra of **SIE10**·Cl (C-I) and **SIE18**·Cl (C-II) in the CH_2 stretching region. (**F**) Variable-temperature X-ray scattering patterns of **SIE14**·Cl showing differences in long- and short-range order for its Iso, LC, C-I, and C-II phases. The intensity between *d* ~6–15 Å is scaled up to make low-intensity peaks visible. Dotted lines are overlaid to aid comparison between spectra.

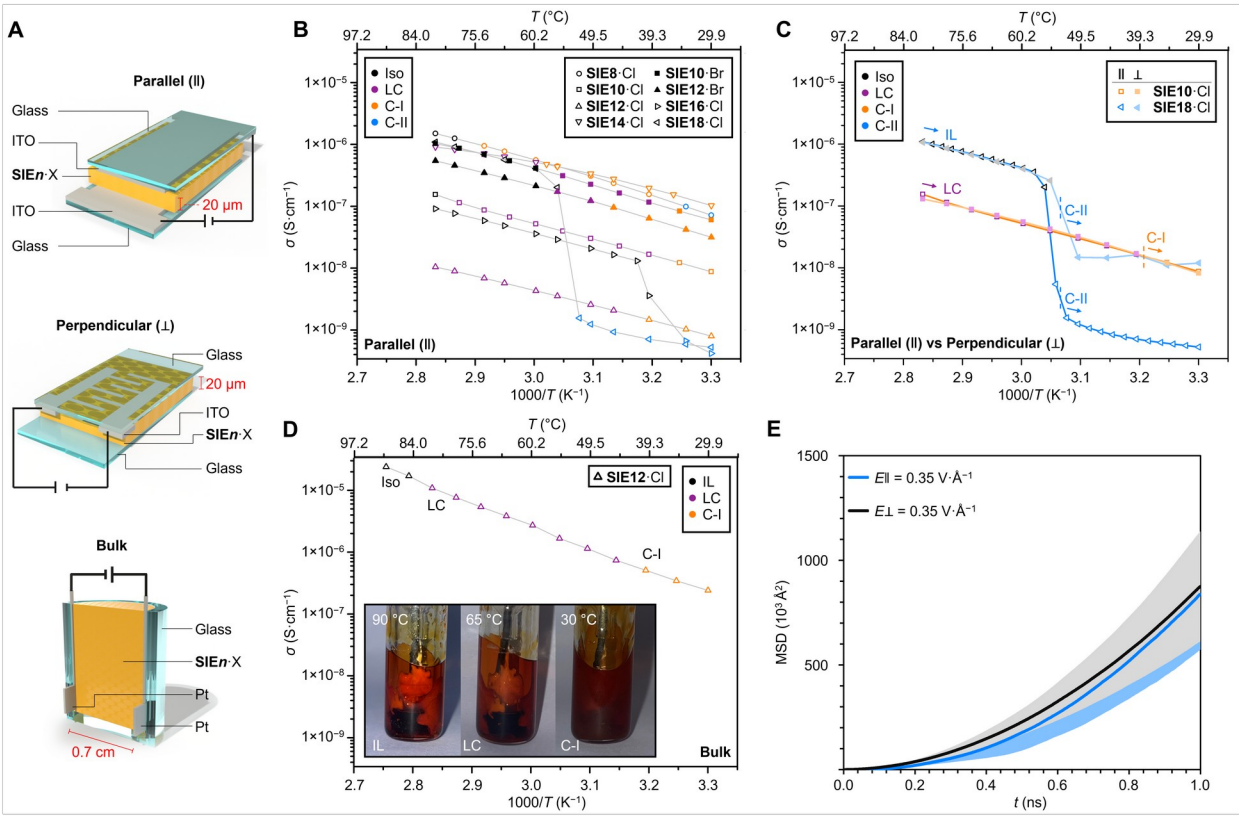

Fig. 3. Dielectric spectroscopy and molecular dynamics simulations reveal the ionic conductivities of the SIE*n*$^+$ salts. (**A**) Schematic diagrams of the cell architectures used to measure permittivities between ITO or Pt electrodes separated by **SIE*n*·**X. (**B**) Arrhenius plot of direct current (DC) ionic conductivity parallel to the alignment of the columnar liquid crystal phase, determined from the 1 kHz plateau in conductance upon applying an alternating current (AC). The **SIE*n*·**X materials that transition from the Iso to LC or C-I phases (*n* = 8, 10, 12, and 14) exhibit continuous Arrhenius behavior across phase boundaries, whereas the longer-chain materials that transition directly from Iso to the C-II phase (*n* = 16 and 18) show a significant drop in conductivity. (**C**) Comparison of conductivities measured parallel and perpendicular to the alignment of the columnar phases showing the isotropic conductivity of **SIE10**·Cl in the LC and C-I phases, which contrasts to the anisotropic conductivity of **SIE18**·Cl in the C-II phase. (**D**) DC conductivity measured using ~0.5 g **SIE12**·Cl in a bulk electrochemical cell with inset photographs showing the visible changes in opacity of the sample following phase transitions. Lines connecting data points are included to guide the eye. All measurements were conducted upon cooling from the Iso state. (**E**) Mean squared displacement (MSD) of Cl^- anions from a MD simulation of the crystal phase of **SIE10**·Cl subjected to external electric fields parallel ($E\parallel$) or perpendicular ($E\perp$) to the column axes.

Table 1. Properties of the SIE*n*·X salts.[a]

	$T_{C\text{-}II}$ (°C)		$T_{C\text{-}I}$ (°C)		T_{LC} (°C)		T_{Iso} (°C)		E_a[d] (eV)
	Heating	Cooling	Heating	Cooling	Heating	Cooling	Heating	Cooling	
SIE8·Cl	20	14	26	36	-[b]	-[b]	79	75	0.54
SIE10·Cl	-[b]	-[b]	11	11	44	40	95	81	0.52
SIE12·Cl	-[b]	-[b]	0	−2	46	44	86	85	0.49
SIE14·Cl	-[b]	-[b]	21	21	71	57	85	83	0.37
SIE16·Cl	-[b]	-[b]	35	-[c]	-[b]	-[b]	50	36	0.48
SIE18·Cl	−45	−62	54	-[c]	-[b]	-[b]	62	55	0.46
SIE10·Br	-[b]	-[b]	6	-[c]	43	40	60	57	0.54
SIE12·Br	-[b]	-[b]	−1	−1	47	46	63	58	0.51

[a]Phase transition temperatures (T_y), where y refers to the phase formed upon heating. Transitions are measured as the onset of signals by DSC. [b]Phase not observed. [c]The cooling T_{Iso} and $T_{C\text{-}I}$ phase transitions are mixed so that the beginning of the $T_{C\text{-}I}$ transition could not be clearly identified. [d]Activation energy barrier to ion diffusion measured from the change in conductivity with temperature observed in thin films using the Arrhenius equation. The value is obtained by fitting data in the linear regime collectively, i.e., for the Iso, LC and C-I phases of **SIE8**·X to **SIE14**·X and for the LC and C-I phases of **SIE16**·Cl and **SIE18**·Cl.